Title: Effect of welding parameters and B_4C contents on the microstructure and mechanical properties of friction stir welded B_4C/6061Al joints

Authors: Y.Z. Li, Q.Z. Wang, B.L. Xiao, Z.Y. Ma

PII: S0924-0136(17)30386-2
DOI: http://dx.doi.org/10.1016/j.jmatprotec.2017.08.028
Reference: PROTEC 15363

To appear in: *Journal of Materials Processing Technology*

Received date: 23-11-2016
Revised date: 19-8-2017
Accepted date: 19-8-2017

Please cite this article as: Li, Y.Z., Wang, Q.Z., Xiao, B.L., Ma, Z.Y., Effect of welding parameters and B4C contents on the microstructure and mechanical properties of friction stir welded B4C/6061Al joints.Journal of Materials Processing Technology http://dx.doi.org/10.1016/j.jmatprotec.2017.08.028

Effect of welding parameters and B_4C contents on the microstructure and mechanical properties of friction stir welded B_4C/6061Al joints

Y.Z. Li[a #], Q.Z. Wang[a*], B.L. Xiao[b], Z.Y. Ma[b*]

a. Key Laboratory of Nuclear Materials and Safety Assessment, Institute of Metal Research, Chinese Academy of Sciences, 72 Wenhua Road, Shenyang 110016, China

b. Shenyang National Laboratory for Materials Science, Institute of Metal Research, Chinese Academy of Sciences, 72 Wenhua Road, Shenyang 110016, China

[#] Now is with Aix-Marseille University, CNRS, IM2NP UMR 7334, 13397, Marseille, France. yuze.li@im2np.fr (Y.Z. Li)

[*] Corresponding author: Tel./fax: +86-24-23971749 (Q.Z. Wang), Tel./fax: +86-24-83978908 (Z.Y. Ma); E-mail address: qzhwang@imr.ac.cn (Q.Z. Wang), zyma@imr.ac.cn (Z.Y. Ma)

Abstract

Annealed 2.8 mm thick B_4C/6061Al composite sheets with various B_4C particle contents (15, 20, 25, 30 wt%) were friction stir welded (FSW) at a tool rotation rate of 1000 rpm and traverse speeds of 50 and 150 mm/min using a single simple-shaped wear-resistant cermet tool. Sound FSW joints were obtained without severe abrasion of the tool. FSW resulted in obvious homogenization and fragmentation of B_4C and the re-distribution of the interfacial products, thereby remarkably increased the hardness of the nugget zone. The hardness profiles of the welded joints were hardly influenced by B_4C contents but significantly by the welding speeds. “S” line and a B_4C depleted region were formed at the top and the bottom of the nugget zone (NZ), respectively. However, they did not deteriorate the mechanical properties of the joints. The tensile strength of all the joints was close or even up to that of the base material with the fracture occurring at the base material.

Keywords: B_4C; Friction stir welding; Composites; Microstructure; Mechanical property.

Introduction

Particle reinforced aluminum matrix composites (PRAMCs) have received significant attentions for aerospace and automotive applications (Clyne and Withers, 1993; Lloyd, 1994), but the poor weldability constraints the wide application of PRAMCs. Ellis (1996) reported that it is very difficult to achieve perfect welding of PRAMCs by means of diffusion welding because of the huge difference between the reinforcement and the matrix alloy. Different welding methods have been employed to weld PRAMCs, such as pulse laser by Dahotre et al. (1991) and friction stir welding (FSW) by Nelson et al. (2000). Among these methods, FSW was proven, by Mishra and Ma (2005) and Wang et al. (2014a), to be a promising method for welding the PRAMCs due to the avoidance of the drawbacks in fusion welding.

However, there were still some key challenges that must be faced in the FSW of PRAMCs. Firstly, Feng et al. (2007, 2008) found that the existence of ultrahard reinforcements in PRAMCs led to severe wear of the steel tool during FSW. This not only results in the difficulty in realizing the long distance welding, but also deteriorates the properties of the FSW joints. Secondly, the much lower plasticity of PRAMCs limited the choice of the welding parameters and easily led to the formation of the welding defects. Recently, Wang et al. (2014b, c) reported sound joints of PRAMCs obtained by FSW, but only for the composites with lower reinforcement content.

As a new kind of reinforcement, B_4C has lower density (about 2.52 g/cm^3) and higher hardness (9.5+ in Mohs' scale) among ultrahard materials (Lee et al., 2001). Viala et al. (1997) considered B_4C particle as an alternative to SiC and Al_2O_3 particles for fabricating advanced

PRAMCs with high stiffness, wear resistance and impact resistance combining with similar thermal stability and chemical inertness. Especially, the specific ability of the B-10 isotope to capture neutrons makes B_4C particle reinforced Al composite (B_4Cp/Al) become an ideal neutron absorbing material in the storage and transportation of spent nuclear fuel (Abenojar et al., 2007; Kang et al., 2010). For this application, welded structures of B_4Cp/Al are required, especially for the B_4Cp/Al with higher B_4C content to obtain higher neutron absorbing ability.

However, the challenges in FSW of the B_4Cp/Al are even tougher for higher hardness of B_4Cp. The investigations on FSW of the B_4Cp/Al are still limited so far. Nelson et al. (2000) used a steel pin to weld the (15-30) wt% B_4Cp/6061Al and found that the screw thread was almost completely eliminated for a welding distance of only 254 mm and a great amount of tool debris was detected in the joint. Kalaiselvan et al. (2013a, b; 2014) used a quadrangular steel pin to weld the (4-12) wt% B_4Cp/6061Al with a maximum welding speed of 140 mm/min. It was reported that the tunnel-like defects were observed at most welding parameters. Guo et al. (2012) and Chen et al. (2009) used a taper pin to weld the B_4Cp/1100Al with 16 and 30 vol.% B_4Cp, and the B_4Cp/6063Al with 6 and 10.5 vol.% B_4Cp. The tool wear was alleviated due to the simple tool shape, and a relatively higher joint efficiency was obtained. From these studies, it can be concluded that low B_4Cp contents, low composite strength, and simple shape of welding tool were beneficial to avoiding the severe tool wear in FSW of the B_4Cp/Al.

The simple-shaped welding tool not only could alleviate the tool wear but also facilitates to the manufacture of welding tool when a high wear resistance material is used. However, the simple-shaped tool is not beneficial to inducing the flow of material during FSW, in which

case the defects may be easily generated. Moreover, for the B_4Cp/Al with higher B_4Cp content, sound welding is still a severe challenge by using the simple-shaped welding tool due to very low plasticity of the composites.

In this study, a new wear-resistant cermet pin with a simple shape (tri-prism, without thread) was used for FSW of the B_4Cp/6061Al with 15-30 wt% B_4Cp at two welding speeds. The aim is (a) to verify the feasibility of conducting multi-pass welding to achieve the perfect FSW joints using a single simple-shaped welding tool and (b) to understand the effect of the welding parameters and the B_4Cp contents on the microstructural evolution and the mechanical properties of FSW joints.

Experimental

The B_4Cp/6061Al composites with the B_4Cp weight fractions of 15, 20, 25 and 30% were fabricated by a powder metallurgy (P/M) technique, using 6061Al alloy with a nominal composition of Al-1.0Mg-0.65Si-0.25Cu (wt%) as the matrix and 7 μm B_4Cp as the reinforcement. The fabrication process of the composites has been described in detail in our previous study (Li et al., 2015a). The composite billets 350 mm in diameter were hot-pressed at 620 °C for 120 min, hot-extruded into planks, and then hot-rolled to sheets 2.8 mm in thickness, which is a typical thickness for the storage and transportation of spent nuclear fuel.

The sheets with a length of 300 mm and a width of 75 mm were butt-welded along the rolling direction using a FSW machine. Based on previous reports (Feng et al., 2008) and our welding trials, a rotation rate of 1000 rpm and welding speeds of 50 and 150 mm/min were selected as the welding parameters in this study. A tool with a shoulder 14 mm in diameter and a tri-prism pin 5 mm in root diameter was made of TiC reinforced Ni cermet. A single

tool was used for the welding of all the composite samples under various FSW parameters with a accumulative total welding distance of ~1200 mm. The FSW samples were designated using a series digital format in Table 1. For example, sample 15-50 denotes that the B_4Cp content of the sample was 15 wt% and the welding speed was 50 mm/min.

Because B_4Cp/6061Al composite is used as neutron absorbing material and the mechanical strength is not the main concerns, the composite sheets were completely annealed (400 °C for 150 min, furnace-cooled) before FSW in orde to reduce the hardness of the composite, thereby modifying the formability of the welds and reducing the tool wear.

After welding, the FSW samples were cross-sectioned perpendicular to the welding direction for microstructural examinations by optical microscopy (OM) and scanning electron microscopy (SEM, quanta 600). Metallographic specimens were mechanically polished to a colloidal 50 nm SiO_2 finish and then etched by Keller's reagent. The phase analyses of the base metal (BM) and the nugget zone (NZ), of the 15-50 and 20-50 joints as the representatives, were conducted using an X-ray diffraction (XRD) analyzer (D/max 2400) with the X-ray wavelength of 1.5406 Å, the aperture size of 10 mm × 1 mm and the step size of 0.04 °/s. The data was processed with MDI Jade 5.0. The interface microstructures of the BM and the NZ, of the 20-50 joint as a representative, were examined by transmission electron microscopy (TEM, TECNAI G2 F20), operating at 200 kV. The thin foils for TEM were prepared by ion-milling technique. Both the analysis surfaces for XRD and TEM were parallel to the sheet surface.

The Vickers hardness profiles of the joints were measured on the cross-sections perpendicular to the welding direction, using a Vickers hardness tester under a 1000 gf load

for 30 s. Dog-bone-shaped tensile specimens with a gauge length of 40 mm and a width of 10 mm were machined perpendicular to the welding direction with the NZ being in the center of the gauge. Room-temperature tensile tests were carried out at a strain rate of 1×10^{-3} s^{-1} and the property data for each condition was obtained by averaging three testing results. The fracture surfaces of the tensile specimens were observed under an SEM.

Results

3.1 Macroscopic morphologies of the tool and welded joints

Fig. 1 shows the macroscopic morphologies of the welding tool before and after welding all the B_4Cp/6061Al samples with various B_4Cp contents under investigated FSW parameters. Obvious abrasion of the pin was observed after about 1200 mm of welding distance, as shown in Fig. 1. However, almost all the abrasion occurred at the ridge of the pin, the head face and the edge planes still maintained the original morphology, and no obvious shortening of the pin was detected. Furthermore, almost no abrasion was detected on the shoulder. This indicates that this simple-shaped cermet welding tool exhibited good wear resistance even for multi-pass welding of eight composite samples.

Fig. 2 illustrates the FSW joints of B_4Cp/6061Al composites with various B_4Cp contents and welding speeds. The surfaces of the joints were characterized by the so-called wake effect as demonstrated (Ceschini et al., 2007), with the presence of semicircular features, similar to those observed in FSW monolithic Al alloys (Cui et al., 2008). The surfaces of all the joints were smooth and no defects were detected in the joints, indicating that sound joining was achieved. The surface quality of the joints did not become worse with the increase of the B_4Cp contents and welding speeds.

3.2 Microstructure of B_4Cp/6061Al composites with various B_4Cp contents

Fig. 3 shows the cross section microstructure of the rolled B_4Cp/6061Al sheets with various B_4Cp contents. It is noted that the B_4Cp exhibited uniform distribution in the matrix for all the composite samples, especially for those with lower B_4Cp contents of 15 and 20 wt% (Fig. 3(a,b)). For the composites with higher B_4Cp contents of 25 and 30 wt%, although the distributions of the B_4Cp were still relatively uniform, inconspicuous clusters with sizes of less than 30 μm appeared (Fig. 3(c,d)). This indicates that the complete uniform distribution of B_4Cp was difficult to obtain when the B_4Cp contents was higher, even after hot rolling. No macro-pores were observed in all composites. The polygonal B_4Cp usually exhibited aspect ratios of larger than 1 and were generally arranged parallel to the sheet surface.

3.3 Macrostructure of B_4Cp/6061Al joints

Fig. 4 shows the cross-sectional macrostructures of the FSW B_4Cp/6061Al joints. No welding defects were detected in the joints under all the investigated B_4Cp contents and welding speeds, indicating that sound FSW joints could be achieved using ultra-hard cermet tool with a tri-prism shaped pin. Similar to most FSW joints of aluminum-based composites (Feng et al., 2008), the NZ in all these FSW B_4Cp/6061Al joints exhibited a basin shape. Unlike in previous reports (Feng et al., 2008), no onion structure was observed in the NZ of all the joints in the present study. The shapes of the NZ were apparently dependent on the welding parameters, not the B_4Cp contents.

For all the FSW joints, the NZ was obviously divided into two sub-zones, NZ-I and NZ-II, as shown in Fig. 4. With increasing the B_4Cp contents, no significant change was observed in the size and shape of the NZ for both two welding speeds. With increasing the

welding speed from 50 to 150 mm/min, the widths of NZ-I were definitely decreased and almost disappeared for all the reinforcement contents (from Fig. 2(a,c,e,g) to (b,d,f,h)). The nugget boundary at the retreating side nearly eliminated when the welding speed was 150 mm/min.

Because similar macrostructures were obtained for the joints with different B_4Cp contents, only one joint with the B_4Cp content of 20 wt% was chosen to subject to more detailed inspection.

Fig. 5(a) shows the macrostructure of the FSW joint with 20 wt% B_4Cp and 50 mm/min welding speed. The "S" line was clearly observed in NZ-II of the joint. It started from the upper surface of the joint and ended at the boundary between NZ-I and NZ-II. Fig. 5(b,d) shows the magnified views of the "S" line after being etched. It can be seen that the "S" line consisted of an array of pits. The formation of the "S" line was proven by Zhang et al. (2013) to be the rearrangement of broken oxide film on the initial butting surfaces. Furthermore, a B_4Cp depleted region was observed at the bottom of NZ-I as shown in Fig. 5(a). Fig. 5(c,e) shows the magnified views of the B_4Cp depleted region. There were only a small number of very fine B_4C particles with a size of less than 200 nm in this region. The width of this region was about 3.5 mm, approximately equal to the width of the bottom of NZ-I and the diameter of the pin head, and the thickness of this region was only about 50 μm.

3.4 Microstructure of B_4Cp/6061Al joints

Fig. 6 shows the microstructures of NZ-I (Fig. 6(b,d,f,h)) and NZ-II (Fig. 6(a,c,e,g)) in the FSW B_4Cp/6061Al joints with various B_4Cp contents at the welding speed of 50 mm/min. Table 2 shows the aspect ratio and long axis value of B_4Cp, calculated from the metallographs,

in the BM, NZ-I and NZ-II of these joints. Three observations can be made. First, more homogeneous distribution of B_4Cp particles was obtained in both NZ-I and NZ-II than that in the BM. The small clusters in the rolled composites with higher B_4Cp contents completely disappeared. The distribution of B_4Cp particles was generally random. The B_4C particles in NZ-I exhibited more homogenous distribution. Second, the cusps of B_4Cp particles were more or less blunted and fine particles were increased in the NZ, especially for the composites with higher B_4Cp contents. These phenomena were much severer in NZ-I than in NZ-II. Third, the mean size and aspect ratio of the particles was definitely decreased in NZ-I. However, the mean size and aspect ratio of the particles in NZ-II were very close to that in the BM.

It was reported in our previous study (Li et al., 2015a) that, when the hot-pressing parameter of B_4Cp/6061Al was 620 °C×2 h, the Mg consumption resulting from interfacial reaction would lead to the deterioration of the age-hardening ability. The age-hardening ability was partially retained when the B_4Cp content was 15 wt%, but nearly exhausted when the B_4Cp content was 20 wt%. Therefore, the B_4Cp/6061Al composites with 15 and 20 wt% B_4Cp were chosen to investigate the effect of FSW on the interfacial reaction in this work.

Fig. 7 shows the XRD patterns of the BM and the NZ of the 15-50 and 20-50 joints. The predominant phases were Al, B_4Cp and Mg_2Si in the 15-50 BM as shown in Fig. 7(a). It is well known that Mg_2Si was the primary precipitate in the 6061Al alloy. Furthermore, Al_3BC and $MgAl_2O_4$ peaks with very weak intensities were also detected in the 15-50 BM. In the NZ of the 15-50 joint, the type and content of the phases did not change compared with those in the BM. As shown in Fig. 7(b), the intensities of the Al_3BC and $MgAl_2O_4$ peaks in the 20-50

BM obviously increased compared with that in the 15-50 BM. However, the intensities of the Mg_2Si peaks were too weak to detect in the 20-50 BM. The XRD patterns of the NZ in the 20-50 joint were similar with that in the BM. However, the content of $MgAl_2O_4$ slightly increased in the NZ.

Fig. 8(a,b) shows the interfacial microstructures of the BM in the 20-50 joint. It can be seen that a large number of interfacial reaction products was located at or close to the B_4Cp/Al interface as pointed by white arrows. Fig. 8(c,d) shows the interfacial microstructures of the NZ in the 20-50 joint. It is noted that the edge of B_4Cp was serrated because of the B_4Cp/Al interfacial reaction (Fig. 8(c)). The reaction products were hardly detected at or close to the interface; however, a lot of reaction products were observed in the region away from the interface as pointed by black arrows in Fig. 8(d).

3.5 Mechanical properties of B_4Cp/6061Al joints

As shown in Figs. 4 and 5, the NZ was obviously divided into two sub-zones for all the FSW joints and the microstructure of the two sub-zones was different. To check the difference in the hardness between NZ-I and NZ-II, the transverse cross-section hardness profiles were measured along the bottom and the top of the 20-50 joint, respectively. As shown in Fig. 9, the distances from both the bottom and the top of the plate to the hardness measurement location were about 600 μm, making the testing line locate in NZ-I and NZ-II respectively. It can be seen that the hardness of NZ-II was higher than that of the BM. However, the average hardness value of NZ-II was only 89 HV, much lower than that of NZ-I in which the average value is about 98 HV. The width of the high hardness zone of NZ-II was about 15 mm, much wider than that of NZ-I, which is just about 7.5 mm.

Fig. 10 shows the transverse cross-section hardness profiles along the bottom of the welded plate with different B_4Cp contents and welding speeds. It can be seen that the hardness values of the BM with different B_4Cp contents were about 60, 80, 90, 110 HV, respectively. The hardness value of NZ-I was much higher than that of the BM and exhibited an inhomogeneous distribution for all the FSW joints. However, the hardness profiles were different with various B_4Cp contents and welding speeds. With the increase of the B_4Cp contents in the B_4Cp/6061Al composites, the hardness profiles could be classified into two categories: one with 15 wt% B_4Cp and the other with the B_4Cp contents no less than 20 wt%.

For the joints with the B_4Cp contents of no less than 20wt% and the welding speed of 50 mm/min, the width of the high hardness zone was about 4 mm, which was equal to the width of NZ-I as shown in Fig. 4. The mean hardness of NZ-I in the 20-50, 25-50 and 30-50 joints were about 98, 120 and 145 HV, respectively. The hardness variations from the BM to NZ-I were 18, 30, 35 HV, increasing with the B_4Cp contents. Beyond NZ-I, the hardness suddenly decreased and approached the level of the BM at the location about 6 mm from the NZ-I center.

For the joints with the B_4Cp contents of no less than 20 wt% and the welding speed of 150 mm/min, the width of the high hardness zone decreased corresponding to the decreased size of NZ-I. The maximum hardness of NZ-I was close to that of the joints with the welding speed of 50 mm/min. However, the hardness decreased gradually to the level of BM with the

increase of the distance from the NZ-I center at the retreating side of NZ-I, which was different from the joints with the welding speed of 50 mm/min.

For the joints with the B_4Cp content of 15 wt% and the welding speed of 50 mm/min, the mean hardness of NZ-I was about 80 HV, with a hardness increase of about 20 HV compared to the BM. Beyond NZ-I, the hardness decreased suddenly to 71 HV, which was still 11 HV higher than the BM and then approached the level of the BM at the distance about 9 mm from the NZ-I center. For the joints with the B_4Cp content of 15 wt% and the welding speed of 150 mm/min, the width of the high hardness zone decreased corresponding to the decreased size of NZ-I and the hardness decreased gradually to the level of BM at the retreating side of NZ-I. Furthermore, the width of the high hardness zone in the joints with 15 wt%B_4Cp was much larger than that of the joints with more B_4Cp.

Fig. 11 shows the tensile properties of the B_4Cp/6061Al composites with various B_4Cp contents and the corresponding FSW joints with two welding speeds. It can be seen that the strength of B_4Cp/6061Al composites increased with the B_4Cp contents and the elongation decreased. The strength of all the weld joints were quite close to that of the BM, indicating the joint efficiency of the FSW joints (defined as UTS_{FSW}/UTS_{BM}) were close to or up to 100%. However, the elongation of all the joints slightly decreased compared with the BM. The “S” line and B_4Cp depleted region observed in the NZ did not affect the mechanical properties of the joints.

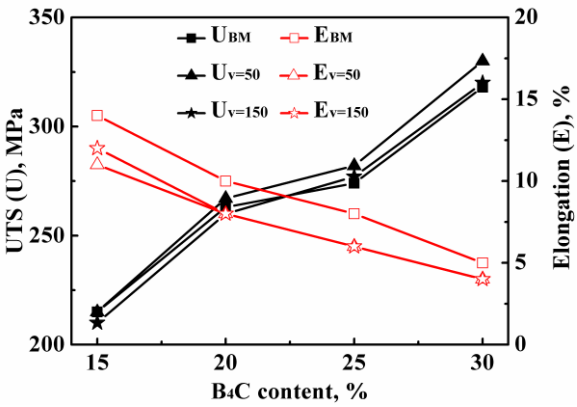

Fig. 11. Tensile properties of FSW B_4Cp/6061Al and weld joints with various B_4Cp contents and welding speeds: 50 mm/min ($U_{v=50}$, $E_{v=50}$) and 150 mm/min ($U_{v=150}$, $E_{v=150}$).

The fracture of all the joints occurred in the BM. Therefore, no obvious differences could be observed on the fracture surface of the BM and the FSW joints with the welding speed of 50 mm/min, as shown in Fig. 12. Similar phenomena were also observed for the FSW joints with the welding speed of 150 mm/min.

Discussion

4.1 Welding tool wear

It is well documented that the severe tool wear is the key factor of inhibiting the engineering applications of FSW for joining PRAMCs. For achieving the engineering application of FSW of PRAMCs, a long-distance welding must be performed using a single tool. It is well known that the tool wear mainly occurred in the initial plunging stage of welding due to low temperature and high deformation resistance of the workpieces (Mishra and Ma, 2005). Therefore, with the same welding distance, multi-pass welding would result in severer tool wear compared to continuous welding.

As shown in Fig. 1, after welding all eight composite samples with an accumulative total welding distance of about 1200 mm, obvious abrasion of the pin occurred only at the ridge of

the pin, the head face and the edge planes still maintained the original morphology without obvious shortening of the pin, and almost no abrasion was detected on the shoulder. This indicates that this simple-shaped cermet welding tool exhibited good wear resistance and is qualified for long-distance welding of B_4Cp/6061Al composites, even the B_4Cp contents was up to 30 wt%. If a continuous welding mode was used, the tool wear would be significantly reduced. Actually, even with this worn tool, it is still possible to achieve high-quality welding, as evidenced by the microstructure and mechanical properties of the FSW joints..

4.2 Macrostructure of the FSW joints

4.2.1 Influence of the welding speeds

The FSW joint was formed by the deformation and flow of the softened material. Because of the effect of both the shoulder and the pin on the material flow, the NZ could be divided in to NZ-II and NZ-I, as shown in Fig. 4. The formation of NZ-I and NZ-II mainly resulted from the effect of the pin and the shoulder, respectively. When a simple-shaped pin was used, the stir ability of the pin was relatively poor (Ilangovan et al., 2015). Thus, the influence of the shoulder was predominant during FSW, resulting in a larger NZ-II.

With the increase of the welding speeds from 50 to 150 mm/min, the effect of the tool, especially the stir effect of the pin with such a simple configuration, was weakened and the friction heat was reduced (Mishra and Ma, 2005). The material per unit volume influenced by the tool would also decrease. Therefore, the width of the NZ was reduced and the nugget boundary at the retreating side nearly eliminated with the increase of the welding speed.

4.2.2 Formation of the B_4Cp depleted region

As shown in Fig. 5, a B_4Cp depleted zone was formed at the bottom of the NZ. This is

attributed to the weakened stir ability of the pin to the material. Zhang et al. (2010) investigated the material flow in the NZ during FSW of 2024Al and suggested a material flow mode around the pin, as shown in Fig. 12. It can be seen that the material close to the pin would flow downward with the rotation of the pin. When a tri-prism pin was used in this study, only very thin material clung to the surface of the pin would flow downward because the driving effect of this pin with the simple shape is very weak. During FSW of composites, the softened aluminum alloy matrix showed much better fluidity than the reinforcing particles. In this case, the matrix clung to the pin would be the main material that flowed downward and filled the hollow under the pin. Therefore, a B_4Cp depleted region was formed at the bottom of NZ-I.

4.3 Microstructure of the FSW joints

4.3.1 Morphology and distribution of B_4Cp

During FSW of the composites, the material in the NZ underwent drastic plastic deformation (Mishra and Ma, 2005). This, combined with the interaction between the reinforcing particles and the pin, led to the fragmentation and homogenization of the particles. Compared with the BM, the smaller size, lower aspect ratio and more uniform distribution of particles were obtained in the NZ, as shown in Fig. 6. A few fine particles were generated because of the fragmentation of the particles.

It is well known that the plastic deformation of the material in the pin affected zone was severer than that in the shoulder affected zone, which also could say severer in NZ-I than in NZ-II in this study. Also, the direct interaction between the pin and the particles occurred in NZ-I. Therefore, the fragmentation and homogenization of the particles in NZ-I were more

obvious than that in NZ-II, as shown in Fig. 6.

4.3.2 Interfacial state

The interfacial reaction in the B_4Cp/6061Al composites has already been proven in our previous studies (Li et al., 2015a, b) with the main interfacial products being Al_3BC and $MgAl_2O_4$. When the hot-pressing parameter was 620 °C×2 h and the B_4Cp content was 20 wt%, all the Mg element was consumed in the interfacial reaction. In this case, there should be no Mg left for possible interfacial reaction during the FSW process. In this case, the content of $MgAl_2O_4$ should be the same between in the NZ and in the BM, as shown in Fig. 7.

TEM examinations showed that most of interfacial products in the BM were located at or close to the B_4Cp/Al interface as shown in Fig. 8(a,b), which is consistent with the previous studies (Li et al., 2015a, b). Because of the drastic plastic deformation and B_4Cp/pin interaction in the FSW process, most of the reaction products were separated from the interface and redistributed in the matrix with deformation and flow of the material during the FSW process, as shown in Fig. 8(c,d). This would facilitate the detection of these products by XRD, resulting in the slight increase of the content of $MgAl_2O_4$ in the NZ, as shown in Fig. 7.

4.4 Mechanical properties of the FSW joints

4.4.1 Hardness of the FSW joints

For the age-hardened aluminum alloys and their composites, both the precipitation state of the matrix and the size and distribution of the reinforcement would change during the FSW process, leading to different hardness variations in different zones of the FSW joint. Thus, the original state of the BM would significantly influence how the hardness of the FSW joints changes. In this study, two types of distinct hardness profiles could be discerned according to

the different interfacial reaction states of the BM.

For the B_4Cp/6061Al composites with no less than 20 wt% B_4Cp, almost all the Mg and Si elements were consumed in the interfacial reaction based on our previous study (Li et al., 2015a), resulting the disappearance of the whole age-hardening ability of those composites. Therefore, the precipitation state of the matrix should barely contribute to the hardness changes in different zones of those FSW joints. The hardness changes of the joints should be mainly attributed to the changes of the size and distribution of the reinforcements, combined with the grain refinement in the NZ.

Even though it was not observed in this study because of the extreme difficulty in obtaining the grain information, the grain refinement in the NZ and relative improvement on the mechanical properties had already been approved by Amirizad et al. (2006) in 15%SiCp/A356 composite and Feng et al. (2008) in 15%SiCp/2009Al composite. As mentioned above, the fragmentation and homogenization of B_4Cp occurred in the FSW joints and much severer in NZ-I. Both the fragmentation and homogenization of the particles would improve the hardness of the composites. Therefore, the NZ exhibited much higher hardness than the BM as shown in Fig. 10(b,c,d) and the hardness of NZ-I was higher than that of NZ-II as shown in Fig. 9. In addition, the interfacial products were broken off and re-distributed in the matrix, as shown in Fig. 8(c,d), would also more or less contribute to the hardness improvement in the NZ.

For the 15 wt% B_4Cp/6061Al composite, Li et al. (2015a) proved that not all the Mg and Si elements were consumed in the interfacial reaction because of the lower content of B_4C and this composite still has obvious age-hardening ability. In this case, the precipitation state

of the matrix would also affect the hardness in different zones of the FSW joint. Generally, the hardness would be the lowest at complete annealing condition for 6061Al (6061Al-O) used in this study.

Cui et al. (2014) claimed that part of large-sized Mg_2Si precipitates would dissolve into the matrix during the FSW process, promoting the hardness by the solution strengthening of these dissolved atoms, as well as the precipitation strengthening due to the formation of a small number of the Mg_2Si precipitates during FSW cooling process. This effect, together with the change in the size of the reinforcements and grains and the distribution of the interfacial products, improved the hardness of the whole FSW joint. Especially, the hardness of the region beyond the NZ was also obviously improved, which was different from the composites with no less than 20wt% B_4Cp. The solution strengthening effect would decrease with the increasing distance from the center of the NZ because of the decreasing plastic deformation of the materials and the heat input. Therefore, the hardness gradually decreased to the level of the BM with increasing the distance from the weld center, as shown in Fig. 10(a).

With the increase of the B_4Cp contents, the homogenization of B_4Cp in the matrix as well as the densification of the composites became more difficult. The possibility of the clusters increased. This could not be eliminated completely even in the subsequent working processes (extrusion and rolling). After the FSW process, almost all the clusters disappeared in NZ-I as shown in Fig. 6, even for the composite with 30 wt% B_4Cp. Therefore, the improvement of the NZ hardness increased with the increase of the B_4Cp contents as shown in Fig. 10.

4.4.2 Tensile properties of the FSW joints

As mentioned above, the hardness of the NZ in all the joints was improved after the FSW process compared to the BM (Figs. 9 and 10). This makes the NZ be the harder zone than the BM. Therefore, during the tension of the FSW joints deformation was concentrated in the BM. In this case, the joint coefficient of the FSW joints were close to or up to 100% with the fracture occurring in the BM.

When evaluating the welded joints, it is a rule to conduct tension of transverse specimens covering various zones of the welds perpendicular to the welding direction. However, considering the fact that the NZ had higher hardness than the BM, evaluating the mechanical resistance of specimens cut along the weld seam is also meaningful. It is expected that the NZ would exhibit higher the mechanical strength than the BM. A detailed study in this aspect will be conducted in the future.

Conclusions

1. Eight B_4Cp/6061Al composites with B_4Cp contents of 15-30 wt% were successfully welded using a single tri-prism shaped cermet pin at welding speeds of 50 and 150 mm/min, obtaining sound FSW joints.
2. After ~1200 mm of accumulative total welding distance, obvious abrasion occurred only in the pin edges, the head face and the edge planes still maintained the original morphology without obvious shortening, and almost no abrasion was detected on the shoulder. This indicates that this tri-prism shaped cermet tool exhibited good wear resistance and is qualified for long-distance welding of B_4Cp/6061Al composites.
3. The NZ was divided into NZ-II (shoulder affected zone) and NZ-I (pin affected zone).

With the increase of the welding speed, the boundary of NZ-I at the retreating side nearly disappeared. A B_4Cp depleted region with a thickness of only 50 μm formed at the bottom of NZ-I.

4. Obvious homogenization and fragmentation of B_4Cp occurred in the NZ. No new interfacial reaction appeared and the contents of the interfacial reaction products did not change obviously in the NZ. However, the interfacial reaction products were broken off from B_4Cp and re-distributed in the matrix.
5. The hardness of the NZ was much higher than that of the BM. With the increase of the B_4Cp contents, the improvement of the NZ hardness increased. With the increase of the welding speed, the width of the high hardness zone decreased.
6. The tensile strength of all the FSW joints was close or even up to that of the BM, with the fracture occurring in the BM. The elongation slightly decreased compared with BM. The "S" line and B_4Cp depleted region exerted no harmful effect on the mechanical properties in the investigated FSW parameters.

Acknowledgments

The authors gratefully acknowledge the support of the National Natural Science Foundation of China under grant No. U1508216.

References

Abenojar, J., Velasco, F., Martínez, M.A., 2007. Optimization of processing parameters for the Al+10% B_4C system obtained by mechanical alloying. J. Mater. Process. Technol. 184, 441-446.

Amirizad, A., Kokabi, A.H., Gharacheh, M.A., Sarrafi, R., Amirkhiz, B.S., Azizieh, M., 2006. Evaluation of microstructure and mechanical properties in friction stir welded A356+15%SiCp cast composite. Mater. Lett. 60, 565-568.

Ceschini, L., Boromei, I., Minak, G., Morrri, A., Tarterini, F., 2007. Effect of friction stir welding on microstructure, tensile and fatigue properties of the AA7005/10 vol.%Al_2O_3p composite. Compos. Sci. Technol. 67, 605-615.

Chen, X.G., da Silva, M., Gougeon, P., St-Georges, L., 2009. Microstructure and mechanical properties of friction stir welded AA6063–B_4C metal matrix composites. Mater. Sci. Eng., A 518, 174-184.

Clyne, T.W., Withers, P.J., 1993. An Itroduction to Metal Matrix Composites. Cambridge University Press.

Cui, G.R., Ma, Z.Y., Li, S.X., 2008. Periodical plastic flow pattern in friction stir processed Al–Mg alloy. Scr. Mater. 58, 1082-1085.

Cui, G.R., Ni, D.R., Ma, Z.Y., Li, S.X., 2014. Effects of Friction Stir Processing Parameters and In Situ Passes on Microstructure and Tensile Properties of Al-Si-Mg Casting. Metall. Mater. Trans. A 45A, 5318-5331.

Dahotre, N.B., McCay, M.H., McCay, T.D., Gopinathan, S., Allard, L.F., 1991. Pulse laser

processing of a SiC/Al-alloy metal matrix composite. J. Mater. Res. 6, 514-529.

Ellis, M.B.D., 1996. Joining of Al-based metal matrix composites - A review. Mater. Manuf. Processes 11, 45-66.

Feng, A.H., Ma, Z.Y., 2007. Formation of Cu_2FeAl_7 phase in friction stir welded SiCp/Al-Cu-Mg composite. Scripta Mater. 57, 1113-1116.

Feng, A.H., Xiao, B.L., Ma, Z.Y., 2008. Effect of microstructural evolution on mechanical properties of friction stir welded AA2009/SiCp composite. Compos. Sci. Technol. 68, 2141-2148.

Guo, J.F., Gougeon, P., Chen, X.G., 2012. Characterisation of welded joints produced by FSW in AA 1100-B_4C metal matrix composites. Sci. Technol. Weld. Joining. 17, 85-91.

Ilangovan, M., Rajendra Boopathy, S., Balasubramanian, V., 2015. Effect of tool pin profile on microstructure and tensile properties of friction stir welded dissimilar AA 6061–AA 5086 aluminium alloy joints. Defence Technology. 11, 174-184.

Kalaiselvan, K., Dinaharan, I., Murugan, N., 2014. Characterization of friction stir welded boron carbide particulate reinforced AA6061 aluminum alloy stir cast composite. Mater. Des. 55, 176-182.

Kalaiselvan, K., Murugan, N., 2013a. Dry sliding wear behaviour of Friction Stir Welded aluminum (6061)-B_4C composite. Int. J. Microstruct. Mater. Prop. 8, 239-251.

Kalaiselvan, K., Murugan, N., 2013b. Role of friction stir welding parameters on tensile strength of AA6061-B_4C composite joints. Transactions of Nonferrous Metals Society of China 23, 616-624.

Kang, P.C., Cao, Z.W., Wu, G.H., Zhang, J.H., Wei, D.J., Lin, L.T., 2010. Phase identification

of Al–B_4C ceramic composites synthesized by reaction hot-press sintering. Int. J. Refract. Met. Hard Mater 28, 297-300.

Li, Y.Z., Wang, Q.Z., Wang, W.G., Xiao, B.L., Ma, Z.Y., 2015a. Effect of interfacial reaction on age-hardening ability of B_4C/6061Al composites. Mater. Sci. Eng., A 620, 445-453.

Li, Y.Z., Wang, Q.Z., Wang, W.G., Xiao, B.L., Ma, Z.Y., 2015b. Interfacial reaction mechanism between matrix and reinforcement in B_4C/6061Al composites. Mater. Chem. Phys. 154, 107-117.

Lloyd, D.J., 1994. Particle-reinforced aluminum and magnesium matrix composites. Int. Mater. Rev. 39, 1-23.

Mishra, R.S., Ma, Z.Y., 2005. Friction stir welding and processing. Mater. Sci. Eng., R 50, 1-78.

Nelson, T.W., Zhang, H., Haynes, T., Friction stir welding of aluminum MMC 6061-boron carbide. , In: II FSW Symposium, Gothenburg, Sweden; 2000.

Viala, J.C., Bouix, J., Gonzalez, G., Esnouf, C., 1997. Chemical reactivity of aluminium with boron carbide. J. Mater. Sci. 32, 4559-4573.

Wang, D., Xiao, B.L., Wang, Q.Z., Ma, Z.Y., 2014. Friction stir welding of discontinuously reinforced aluminum matrix composites – a review. Acta Metall. Sinica – Eng. Lett 27, 816-824.

Wang, D., Wang, Q.Z., Xiao, B.L., Ma, Z.Y., 2014. Achieving friction stir welded SiCp/Al-Cu-Mg composite joint of nearly equal strength to base material at high welding speed. Mater. Sci. Eng., A 589, 271-274.

Wang, D., Xiao, B.L., Wang, Q.Z., Ma, Z.Y., 2014. Evolution of the microstructure and

strength in the nugget zone of friction stir welded SiCp/Al-Cu-Mg composite. J. Mater. Sci. Technol. 30, 54-60.

Zhang, Z., Xiao, B.L., Ma, Z.Y., 2013. Effect of segregation of secondary phase particles and "S" line on tensile fracture behavior of friction stir-welded 2024Al-T351 joints. Metall. Mater. Trans. A 44A, 4081-4097.

Zhang, Z., Xiao, B.L., Wang, D., Ma, Z.Y., 2010. Effect of alclad layer on material flow and defect formation in friction-stir-welded 2024 aluminum alloy. Metall. Mater. Trans. A 42, 1717-1726.

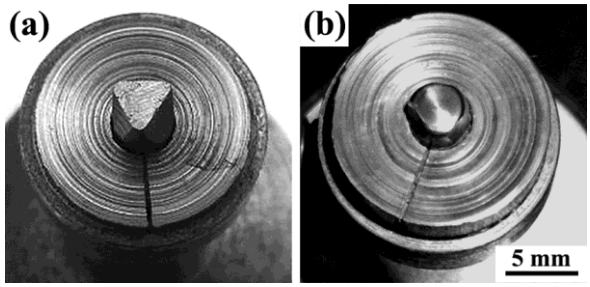

Fig. 1. The morphologies of welding tool (a) before and (b) after welding all B_4Cp/6061Al samples with a welding distance of ~1200 mm.

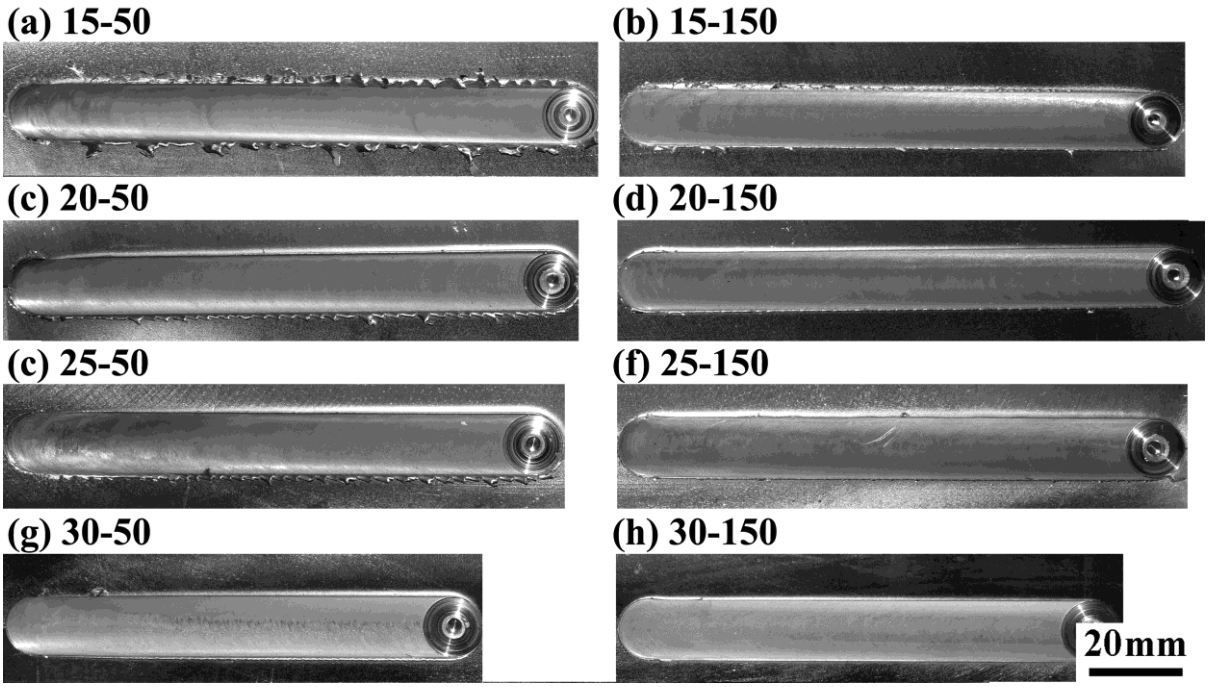

Fig. 2. The surface morphologies of FSW B_4Cp/6061Al joints.

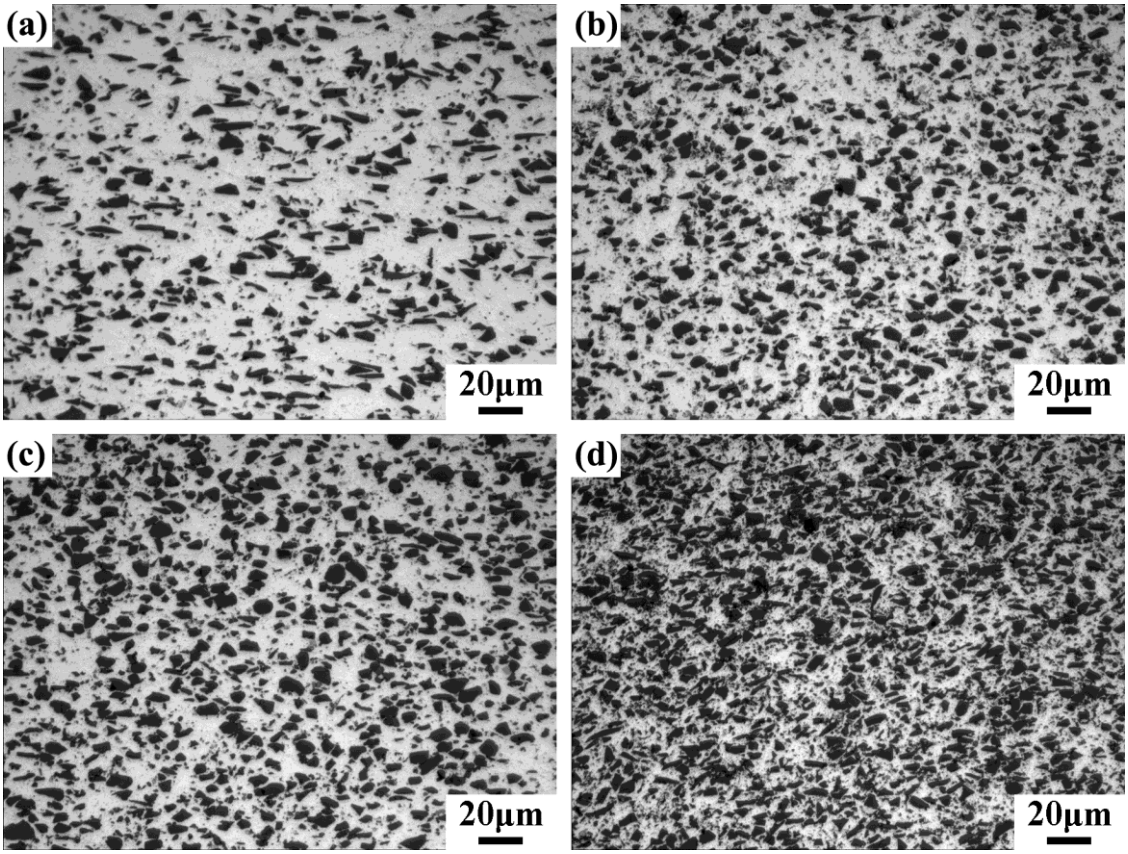

Fig. 3. Optical micrographs of rolled B_4Cp/6061Al composites with B_4Cp contents of (a) 15 wt%, (b) 20 wt%, (c) 25 wt%, and (d) 30 wt%.

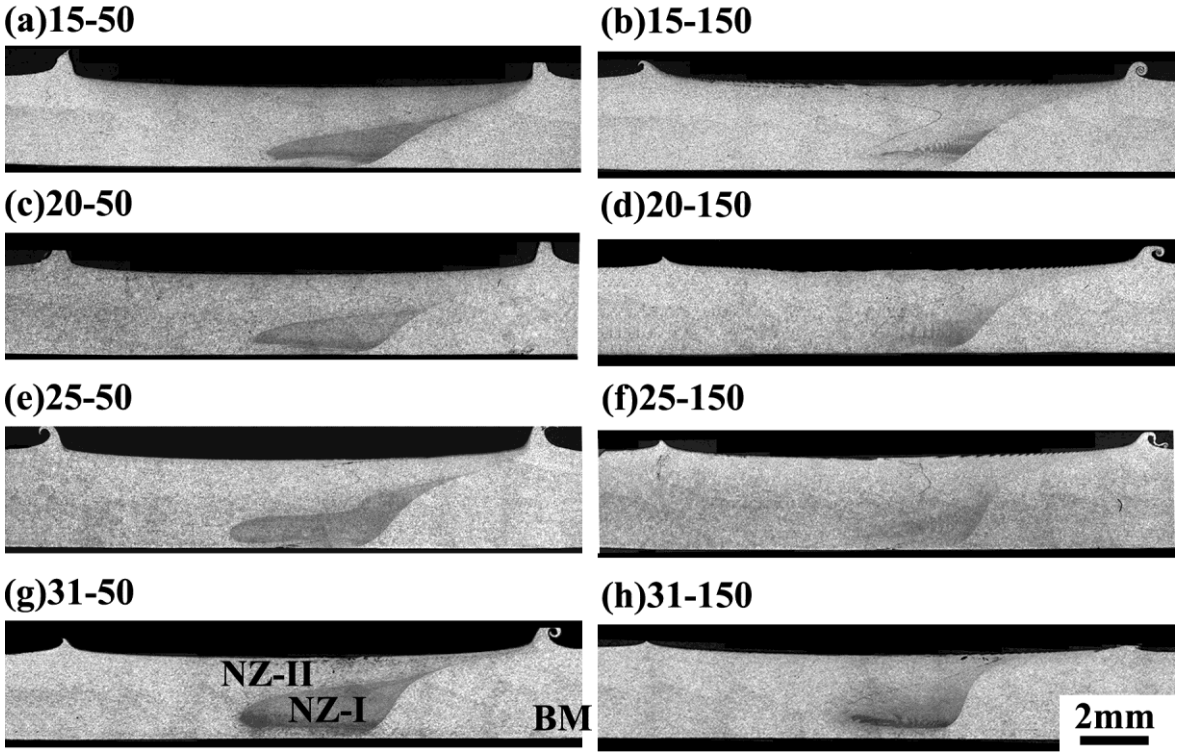

Fig. 4. Cross-sectional macrostructures of FSW B_4Cp/6061Al joints (The advancing side on the right).

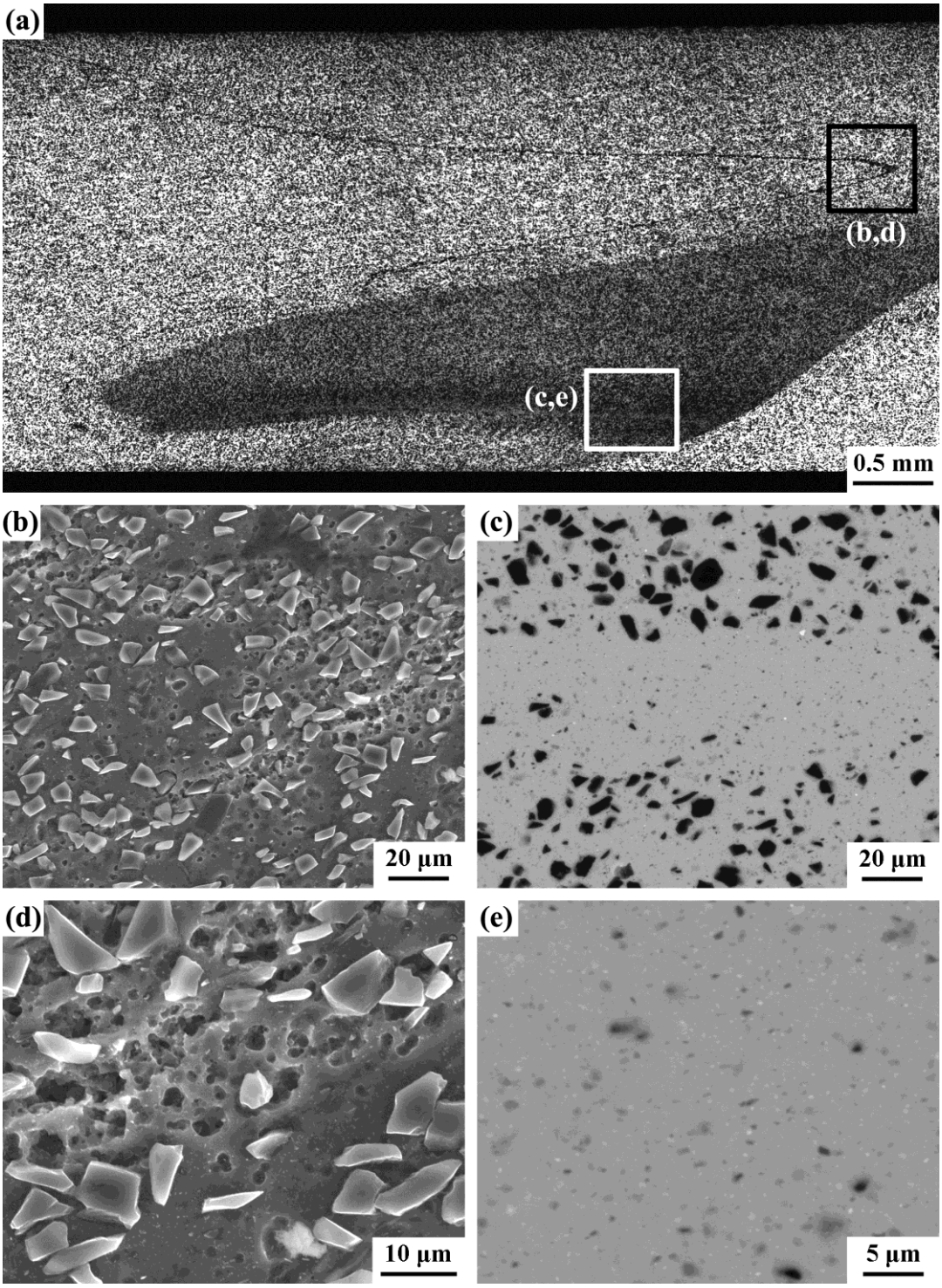

Fig. 5. (a) Cross-sectional macrostructures of 20-50 joint showing existence of "S" line and B_4C depleted region; magnifed view of (b, d) "S" line and (c, e) B_4C depleted region after being etched.

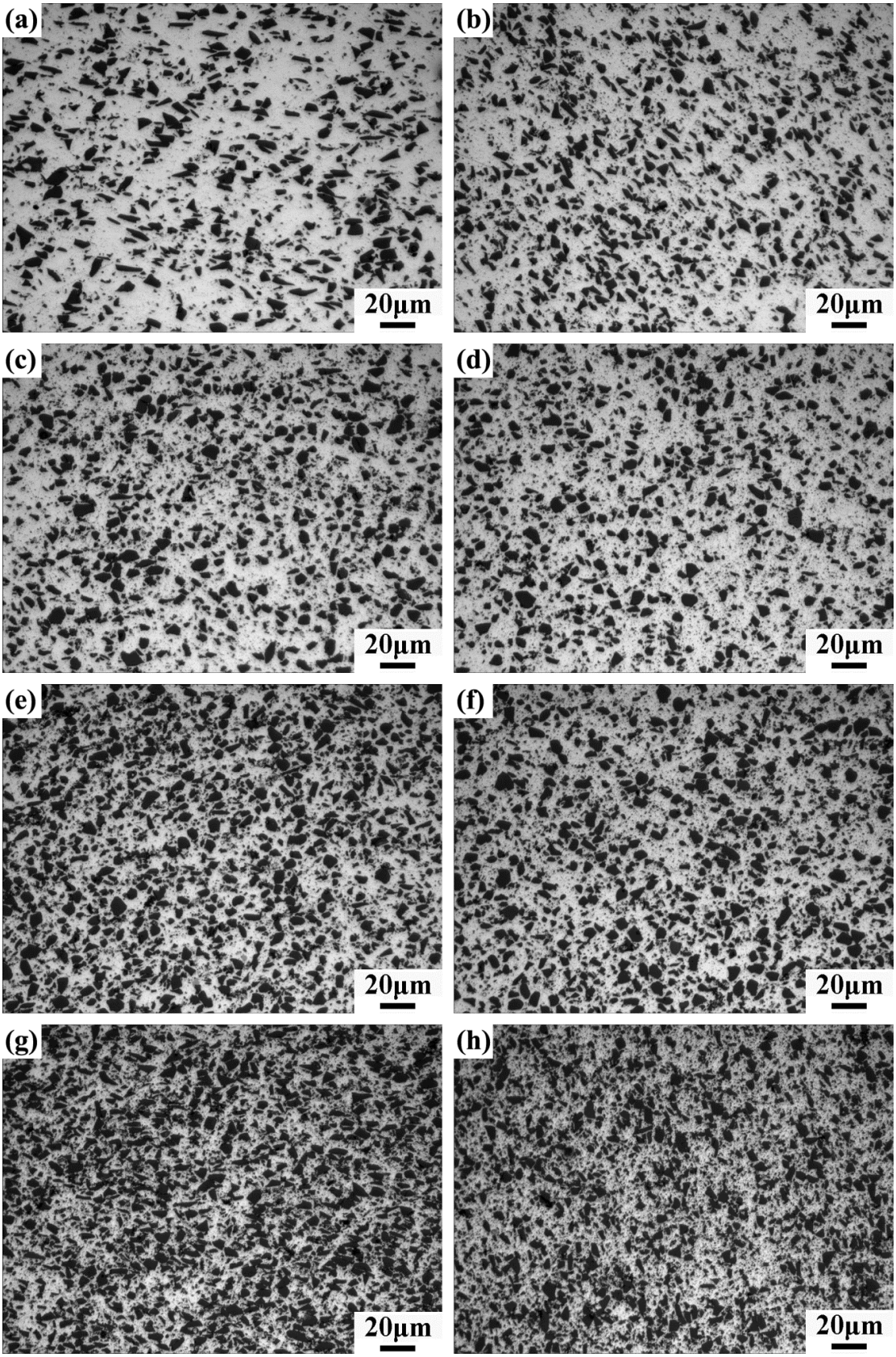

Fig. 6. Optical micrographs of B_4C/6061Al joints, NZ-II: (a) 15-50, (c) 20-50, (e) 25-50, (g) 30-50; NZ-I: (b) 15-50, (d) 20-50, (f) 25-50, (h) 30-50.

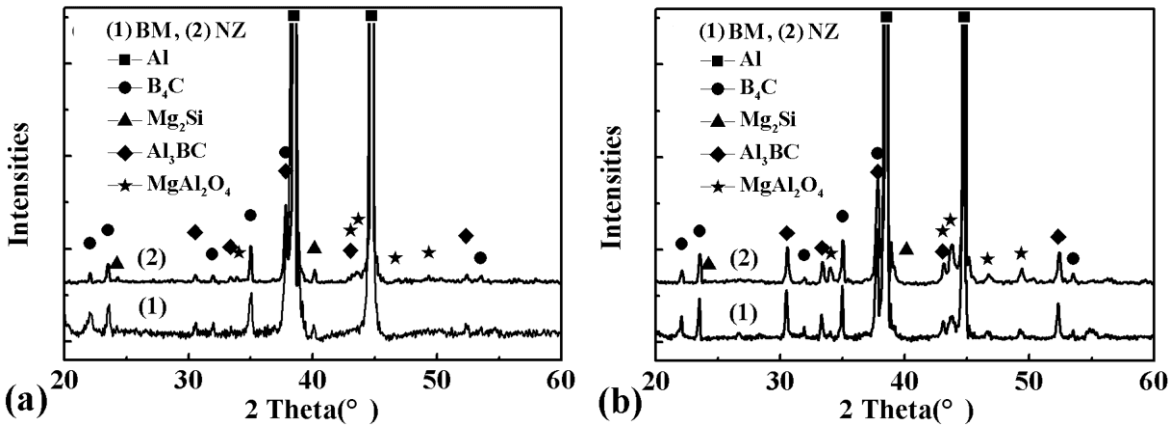

Fig. 7. XPD patterns of (a) 15-50 and (b) 20-50 joints.

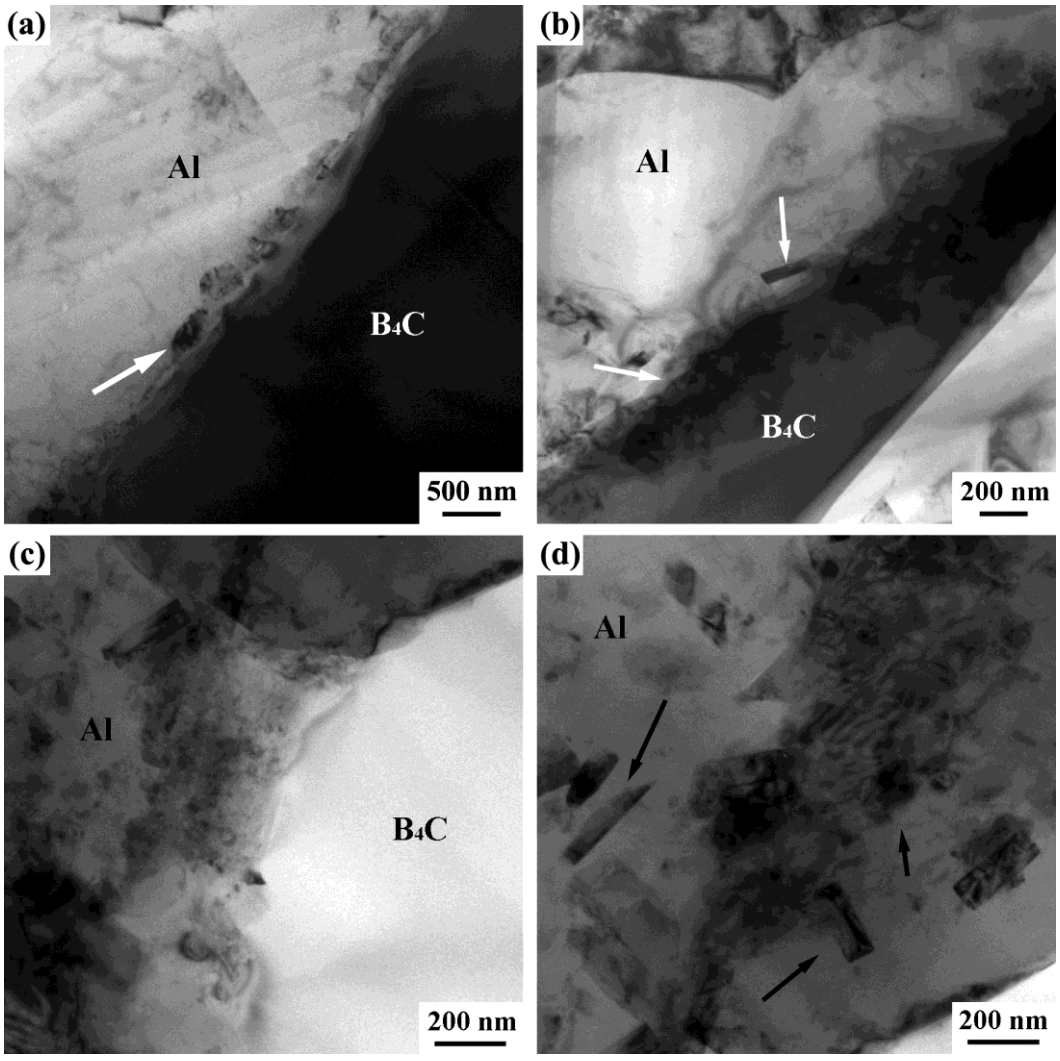

Fig. 8. B_4Cp/Al interfacial microstructures of (a,b) BM and (c,d) NZ-I in FSW 20 wt%B_4Cp/6061Al joint

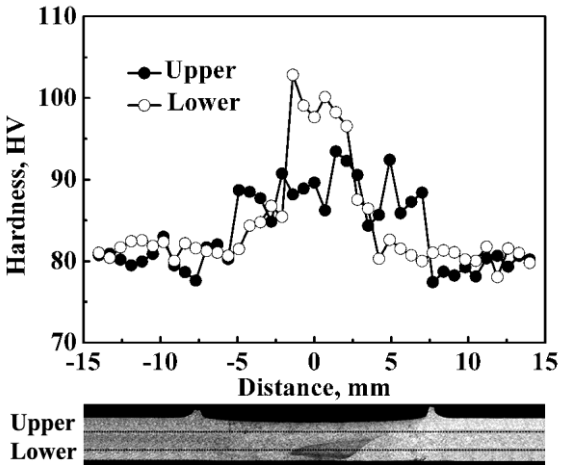

Fig. 9. Hardness profiles along the transverse section of 20-50 joint.

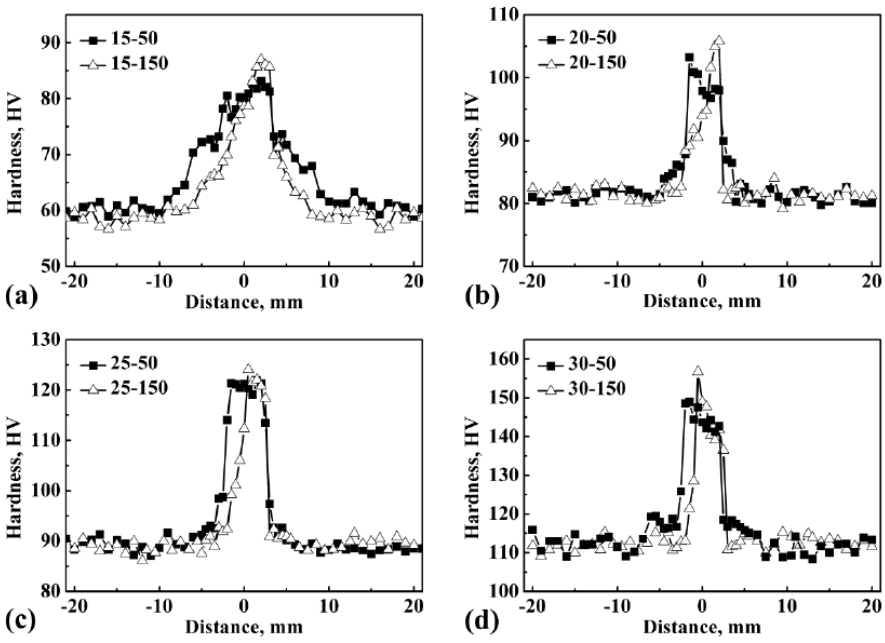

Fig. 10. Hardness profiles of the transverse section of the joints.

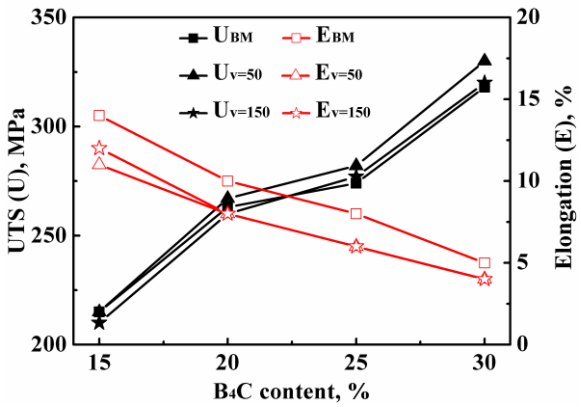

Fig. 11. Tensile properties of FSW B_4Cp/6061Al and weld joints with various B_4Cp contents and welding speeds: 50 mm/min ($U_{v=50}$, $E_{v=50}$) and 150 mm/min ($U_{v=150}$, $E_{v=150}$).

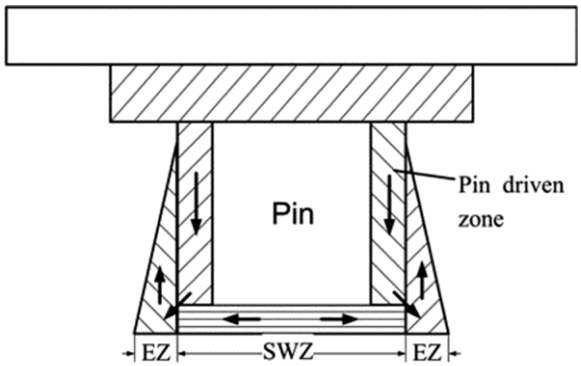

Fig. 12 Schematic diagram for welding formation during FSW: EZ denotes excess material zone and SWZ denotes swirl zone (Zhang et al., 2010).

Table 1. Designations of FSW B_4Cp/6061Al samples

Samples	Particle content, wt%	Welding speed (υ), mm/min	Designation
1	15	50	15-50
2	15	150	15-150
3	20	50	20-50
4	20	150	20-150
5	25	50	25-50
6	25	150	25-150
7	30	50	30-50
8	30	150	30-150

Table 2. The aspect ratio and long axis value of B_4Cp in BM, NZ-I and NZ-II of various joints

Joints	Regions	Aspect ratio	Long axis, μm
	BM	2.49	10.07
15-50	NZ-I	2.06	9.14
	NZ-II	2.21	10.02
	BM	1.94	9.48
20-50	NZ-I	1.84	8.47
	NZ-II	1.92	9.42
	BM	1.78	7.43
25-50	NZ-I	1.61	6.83
	NZ-II	1.69	7.20
	BM	1.90	6.97
30-50	NZ-I	1.67	6.48
	NZ-II	1.85	6.85

Table 3. Tensile properties of FSW B_4Cp/6061Al joints with various B_4Cp contents and welding speeds

Samples	EL, %	UTS of joint, MPa	UTS of BM, MPa	EL of BM, %	UTS_{FSW}/UTS_{BM}, %	Fracture location
15-50	11	215	215	14	100	BM
15-150	12	210	215	14	97	BM
20-50	8	267	263	10	100	BM
20-150	8	260	263	10	99	BM
25-50	6	282	274	8	100	BM
25-150	6	277	274	8	100	BM
30-50	4	330	318	5	100	BM
30-150	4	320	318	5	100	BM